



## Article

# New Insights into the Internal Structures and Geotechnical Rock Properties of the Giant San Andrés Landslide, El Hierro Island, Spain

Jan Klimeš<sup>1,\*</sup>, Yawar Hussain<sup>2</sup>, Anne-Sophie Mreyen<sup>3</sup>, Léna Cauchie<sup>4</sup>, Romy Schlögel<sup>5</sup>, Valentine Piroton<sup>5</sup>, Matěj Petružálek<sup>6</sup>, Jan Blahůt<sup>1</sup>, Miloš René<sup>1</sup>, Stavros Meletlidis<sup>7</sup> and Hans-Balder Havenith<sup>5</sup>

<sup>1</sup> Institute of Rock Structure & Mechanics, Czech Academy of Sciences, V Holešovičkách 41, 18209 Prague, Czech Republic

<sup>2</sup> Earth Sciences Department of Sapienza University of Rome, Research Center for Geological Risks (CERI), 00185 Rome, Italy

<sup>3</sup> Urban and Environmental Engineering, Faculty of Applied Sciences, University of Liege, 4000 Liege, Belgium

<sup>4</sup> Faculty of Sciences, University of Liege, 4000 Liege, Belgium

<sup>5</sup> Department of Geology, Faculty of Sciences, University of Liege, 4000 Liege, Belgium

<sup>6</sup> Institute of Geology, Czech Academy of Sciences, Puškinovo náměstí 447/9, 16000 Prague, Czech Republic

<sup>7</sup> Centro Geofísico de Canarias, Instituto Geográfico Nacional, Calle La Marina 20, 38001 Santa Cruz de Tenerife, Spain

\* Correspondence: klimes@irms.cas.cz

**Abstract:** The San Andrés landslide on El Hierro (Canary Islands) represents a rare opportunity to study an incipient volcanic island flank collapse with an extensive onshore part. The presented research improves the knowledge of the internal structure and rock characteristics of a mega-landslide before its complete failure. The investigation combines multiple geophysical measurement techniques (active and passive seismic) and remotely sensed, high spatial resolution surveys (unmanned aerial vehicle) with in situ and laboratory geotechnical descriptions to characterize the rock properties inside and outside the San Andrés landslide. The available geophysical and geological data have been integrated into 3D geomodels to enhance their visual interpretation. The onshore geophysical investigations helped detect the possible San Andrés landslide sliding surfaces at depths between 320 m and 420 m, with a rather planar geometry. They also revealed that rocks inside and outside of the landslide had similar properties, which suggests that the previous fast movements of the landslide did not affect the bulk properties of the displaced rocks as the failure chiefly occurred along the weakened sliding plane. Uniaxial strength tests on basalt rocks further indicate a high variability and spatial heterogeneity of the rock strength properties due to the different types of volcanic rocks and their texture. The new information on the rock properties and structural setting of the San Andrés landslide can now be used to develop realistic geotechnical slope models of the onshore part of the flank collapse that are possibly applicable for slope stability or deformation calculations. It will also help assess related hazards marked by a low occurrence probability and a high impact potential.

**Keywords:** giant landslides; seismic refraction tomography; seismic ambient noise; UAV; geological strength index



**Citation:** Klimeš, J.; Hussain, Y.; Mreyen, A.-S.; Cauchie, L.; Schlögel, R.; Piroton, V.; Petružálek, M.; Blahůt, J.; René, M.; Meletlidis, S.; et al. New Insights into the Internal Structures and Geotechnical Rock Properties of the Giant San Andrés Landslide, El Hierro Island, Spain. *Remote Sens.* **2023**, *15*, 1627. <https://doi.org/10.3390/rs15061627>

Academic Editor: Sandro Moretti

Received: 20 January 2023

Revised: 11 March 2023

Accepted: 13 March 2023

Published: 17 March 2023



**Copyright:** © 2023 by the authors. Licensee MDPI, Basel, Switzerland. This article is an open access article distributed under the terms and conditions of the Creative Commons Attribution (CC BY) license (<https://creativecommons.org/licenses/by/4.0/>).

## 1. Introduction

Onshore and submarine landslides around volcanic islands are among the Earth's largest known mass movements [1]. The database of volcanic island flank collapses contains 182 documented cases among which more than 20 mega-landslides have occurred on the Canary Islands during the past 300 ka (Figure 1, [2]). Recent studies from the same archipelago [3–6] propose multiple-stage collapses or slip events pointing toward the possible reactivation of apparently inactive structures. These findings argue for the careful



A promising geophysical method potentially describing the rock environment properties to greater depths (up to hundreds of meters) is based on seismic ambient noise measurements [15,16], which are very small amplitude vibrations [17]. In recent years, ambient noise single seismic stations (H/V or HVSR, horizontal-to-vertical spectral ratio technique) and multiple seismic stations (seismic arrays) have been extensively adopted as they represent effective tools to characterize the elastic properties of the subsoil and detect seismic wave velocity changes with depth. In particular, small-aperture seismic arrays using multiple stations can be used to describe the rock environment at great depths (up to hundreds of meters). Ensuring the reliability of results inferred from these passive seismic methods remains a challenging task that has been tackled either through the adaptation of multiple geophysics techniques [18–20] or by including the results from remote sensing [13]. The aforementioned methods can also be used to investigate deeper parts of landslide bodies, depending on the frequency contents of the recorded ambient noise data and the degree of deformation in the strata (not violating the 1D assumption), typically in combination with active seismic methods, especially seismic refraction tomography (SRT) and multi-channel analysis of surface waves (MASW) [20]. The integration of active, passive, and UAV-aided (unmanned aerial vehicle) deformational and survey planning investigation over a giant volcanic flank collapse can be quite promising, however, the literature is limited to their applications in the subsurface characterization of volcanoes, as described by [21].

When working with a large amount of geophysical and geological data describing rock environments at different depths, data integration in the form of 3D geomodels represents a key task to visualize and analyze diverse surface and subsurface information as well as comprehend their spatial relationships. 3D geomodelling applications include, amongst others, structural modeling [22,23], reservoir characterization (petroleum engineering), and hydrogeological engineering [24]. Applications in the field of geohazard assessment are less frequent; however, geomodels of large landslides possibly enhance the understanding of these complex sites and represent valuable input information for further numerical or physical computations [19,25,26].

There are only three volcanic islands known to host mega-landslide features that have not failed completely. One is the episodically reactivated Hilina Slump on the Hawai'ian Islands [27], the other is a slump on Pico Island in the Azores [28], and the third is the partly failed San Andrés landslide (SAL) on El Hierro, Canary Islands [10]. The latter provides a rare opportunity to study a partly failed, onshore mega-landslide, in which rocks and major failure planes are exposed within a 900 m-long abandoned water gallery. Therefore, not only do indirect geophysical methods allow for the study of deep sub-surface rock properties, but direct, in situ, and laboratory rock characterization can be deployed. Such a field setting calls for research to (i) describe the rock environment within and outside the SAL; (ii) identify the depth and shape of onshore sliding planes using the aforementioned geophysical methods; and (iii) characterize the SAL rock strength properties by laboratory testing, in situ evaluation, and geophysical prospection. Such data can serve to improve our knowledge on the possible internal structure and characteristics of mega-landslides before their catastrophic failures, and thus significantly improve our ability to reliably assess the hazard of these rare, but potentially highly damaging phenomena.

## 2. Study Area

### 2.1. Geological Settings

El Hierro is an active volcanic edifice and the youngest of the eight Canary Islands [6,29–31]. It emerges from the 3700 m deep ocean floor and reaches a maximum altitude of 1502 m [32]. The volcano-tectonic model of El Hierro suggests a rather uniform stress field during the growth of the whole island, resulting in the radial distribution of the major structural elements [33]. Its oldest subaerially exposed rocks (e.g., basaltic and tephritic flows) are represented by the Tiñor Unit (Figure 1). Their maximum age was estimated to 1.12 Ma [34]. This unit is thought to have developed rapidly until around the time of the Tiñor debris

avalanche at 0.88 Ma [35]. The rocks of the El Golfo-Las Playas Unit (e.g., basaltic, trachy-basaltic, and tephritic flows), with a maximum age of 0.55 Ma [34], overlaid much of the Tiñor Unit and infilled the scarp area of the Tiñor debris avalanche [14]. The youngest rocks are represented by the Rift Series (e.g., trachybasaltic, basanitic, and tephritic flows with basaltic tephra cones), which have a maximum age of 0.16 Ma [34]. Over the past 33,000 years, onshore eruptions have reoccurred approximately once every 1000 years [35], with the most recent and ongoing phase of volcanism beginning at around 2.5 ka [14,36]. Since then, all of the rift systems on the island have been active intermittently, with the lava flows being similar in composition to those of the El Golfo Unit [37]. This phase of rift volcanism is characterized by monogenetic volcanism with eruptions of mafic magmas forming cinder cones and lava flows [14]. Recently, a period of intense seismic activity lasted from July 2011 [38] until 2014 [39], which was accompanied by an offshore eruption from October 2011 to March 2012 [40].

The three-point star shape of El Hierro is a result of at least seven gravitational slope failures identified up until now (Figure 1) [2,5,14,41–49]. The formation of these landslides possibly conditioned the local stress field witnessed by the observed NE–SW and N–S directions of the structural elements in the shallower parts of the El Hierro edifice [33]. Large slope failure, considered as a slump by [50], or as a deep-seated gravitational slope deformation by [51], here referred to as the San Andrés landslide (SAL), is defined by a group of pronounced landslide detachment planes previously termed as faults [10]. Similar features have been described from other volcanic islands including the Azores [28] and the Hawai’ian Islands [52]. The submarine part of the SAL is composed of chaotic landslide deposits most likely superimposed over deformed strata [45,53]. It has previously been proposed that the SAL is an anchored block associated with the (mostly subaquatic) debris avalanche at Las Playas I [10].

## 2.2. The San Andrés Landslide (SAL)

The San Andrés landslide has developed in the rocks of the Tiñor Unit (Figure 1). This unit incorporates three distinct subunits: the basal subunit comprises relatively thin, 20–40 cm, steeply dipping lava flows; the intermediate subunit, which forms the majority of the unit, comprises thicker, up to 4 m, shallow dipping lava flows; and the third subunit is formed by emission vents with well-preserved craters and associated lavas [54]. The broad arcuate failure surface system, which defines the boundaries of the landslide mass to the northeast, is terminated to the southwest by an escarpment associated with the debris avalanches at Las Playas. Geological evidence suggests that the landslide mass is moving progressively to the east and southeast [55], while creep, in the order of 0.3 mm/yr, has recently been detected at its main detachment plane [56]. A possibly retrogressive failure plane was described 900 m inland from the main entrance of the abandoned water gallery (Figure 2) and developed in fractured olivine-pyroxene massive basalts with well-preserved sub-vertical slickensides and a soft clay infill [51].

The analysis of the topographic and bathymetric data (for the data description, see Section 3.5) revealed that the subaerial part of the landslide has a width of about 8 km and a length of about 2 km, while its submarine portion has a maximum width of more than 12 km and extends for at least 15 km, reaching a depth of 2900 m. Its subaerial slopes are on average inclined by  $16.5^\circ$ , while its submarine slopes are inclined, on average, by less than  $10^\circ$  [57,58]. The onshore landslide mass is divided into several swathes by antithetic faults [48]. One of these antithetic faults appears to be responsible for the development of an extensional trench, with a width of approximately 300 m, below the main detachment plain. Furthermore, the landslide mass is dissected by a series of deeply entrenched gullies, with a relative relief of more than 200 m, oriented northwest to southeast. These gullies delineate large blocks whose elevations tend to decrease toward the north-eastern margin of the landslide [51]. The offshore part of the landslide exhibits a large number of ridges and blocks, but it does not present any morphological evidence for submarine debris flows,

turbidity currents, or other sedimentary accumulations similar to those associated with the failures at the El Golfo and El Julan landslides.

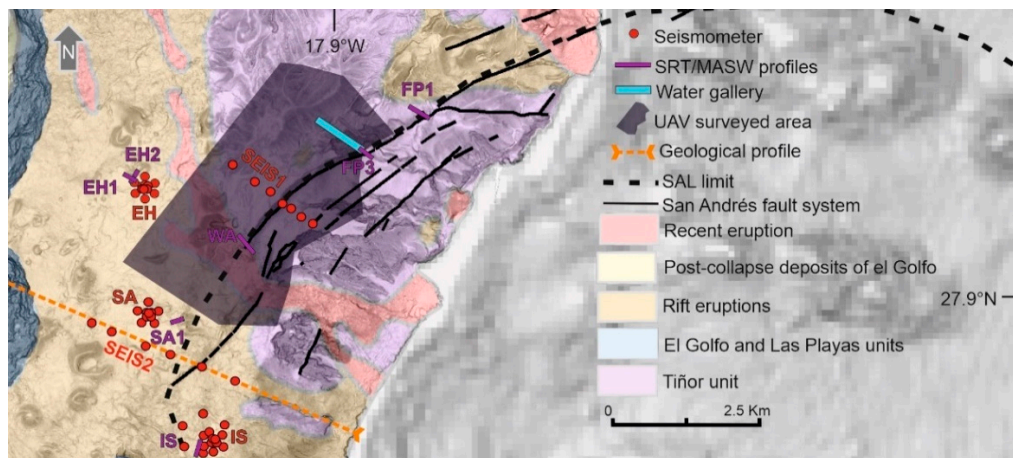


**Figure 2.** Location of the 2020 and 2021 geophysical and UAV survey sites plotted on the geological map (for legend, see Figure 1). The survey sites are EH—El Hierro, SA—San Andrés, IS—Isora, FP—Fault Plane, and WA—West Andres sites.

A recent investigation of the outcropping SAL detachment plane [6] revealed that the steeply dipping failure surface is composed of a striated frictionite. Its microstructural analysis and the kinematic markers on the failure surface evidence two separate slip events. Their cosmogenic  $^3\text{He}$  exposure ages show that the first slip event occurred between 545 ka and 430 ka while the second one most likely occurred between  $183 \pm 17$  and  $52 \pm 17$  ka [6].

### 3. Methods

The present study utilized the benefits of active and passive seismic methods for the detection and characterization of sliding surface(s) as well as the determination of the degree of the deconsolidation of the sliding mass of the SAL. A combination of methods was selected to be able to investigate both the near-surface (with more detail) as well as the deeper (tens to hundreds of meters) elastic rock properties and contrasting interfaces within and outside the SAL. We applied active multichannel analysis of surface waves (MASW) and seismic ambient noise techniques using the dispersive properties of the surface waves for soil stiffness estimation and active seismic refraction tomography (SRT) to map the P-wave velocity ( $V_p$ ) distribution of the ground. The geographic coordinates of the installed instruments (geophones and seismometers) were taken with a Topcon<sup>®</sup> DGPS system.

#### 3.1. Passive Seismic Measurements

In October 2020, we employed seven broadband velocimeters CMG-6TDs with a flat response down to 0.03 Hz with a sampling frequency set to 200 Hz. Three seismic arrays and two linear profiles were deployed inside and outside the SAL (Figure 2). One array used seven broadband velocimeters CMG-6TDs with a flat response down to 0.03 Hz and a sampling frequency set to 200 Hz.

The array geometries (EH, SA, IS) consisted of two or three circular configurations around a central fixed station with increasing inter-station distances. The EH and SA arrays consisted of two hexagonal configurations of 50 and 200 m, respectively; the IS array was composed of one pentagonal shape with inter-station distances of 50 m and two hexagonal configurations with inter-station distances of 200 m and 400 m, respectively. To avoid important topographic effects in the measurements, we kept the network of seismometers on a relatively flat area. The configuration of the 400 m array was therefore shifted with respect to the two smaller ones due to the vicinity of the cliffs.

### 3.1.1. Horizontal-to-Vertical Spectral Ratio Technique (H/V)

The H/V technique [59] estimates the fundamental resonance frequencies from measured seismic ambient noise using a single seismic station. It enables the identification of impedance contrasts at depth in a given site. It uses the three-component seismic signals (E–W, N–S, and vertical) at each measurement point by computing the spectral ratios between the horizontal and the vertical components.

We first pre-processed the signals by (i) applying a bandpass filter between 0.2 and 20 Hz, and (ii) eliminating the transient signals by applying the STA/LTA technique ([60]; STA = 2 s, LTA = 30 s, STA/LTA = 3.5). The H/V analysis was performed on 40-s-long signal windows sliding the entire recordings; the final H/V curve was obtained by averaging the results of the single 40-s-long windows. Examples of H/V curves for the four sites are shown in Figure S1.

After estimating the fundamental resonance frequencies ( $f_0$ ) as the peak observed at a lower frequency, the depths of the impedance contrasts were derived for simple geological structures using the well-known equation relating the depth of the deposits to their fundamental frequency, and their shear wave velocity ( $V_s$ , [60]). The resonance frequencies were first estimated at each measurement point of the three arrays and two profiles with a measurement duration from 2 to 7 h, while the corresponding  $V_s$  were determined with the multi-station array (see below).

### 3.1.2. Ambient Noise Surface Wave Dispersion (Seismic Multichannel Array)

We applied the high-resolution frequency-wave number (f-k) analysis [61,62] on the vertical components of the seismic data recorded simultaneously at the seismic arrays (IS, EH, and SA) to retrieve the Rayleigh dispersive properties of the surface waves. For each site and each configuration, a dispersion curve was computed (phase velocity as a function of frequency). We then combined the curves at each site in one final curve that became the target of the inversion process. Each dispersion curve was defined in its domain of validity, and defined by the minimum and maximum resolvable wavelengths, which were determined according to the array geometry [15].

Inversion of the dispersion curves led to the estimation of  $V_s$  as a function of depth, enabling the identification of contrasts in the rock properties. The inversion was performed using a neighborhood algorithm (Dinver module of Geopsy software 3.4.2, [63]), which enabled the search for the best model in the parameter space defined by the thickness and  $V_s$  for a layered model that will represent the site under investigation. Together with the number of layers, the thickness and the shear-wave velocities in each layer are the main parameters that influenced the dispersion curves the most [64].

## 3.2. Active Seismic Measurements

The active seismic survey comprised data interpretation in terms of seismic refraction tomography (SRT) and multi-channel analysis of surface waves (MASW). For this survey, 48 vertical geophones of the natural frequency at 4.5 Hz were fixed to the ground, forming a linear array configuration with 5 m inter-geophone spacing. In total, seven SRTM profiles of a maximum profile length of 235 m were set up (Figure 2) and signals were recorded with two 16-bit, 24-channel, DAQLink-IV (Georeva<sup>®</sup>) seismographs; sledgehammer shots were used as the source of the seismic waves. The signal-to-noise ratio was improved by stacking five shots at each source location.

The acquired traces of each shot location were processed by first using waveform normalization and filtering to improve the phase arrival clarity. Then, the first arrivals were picked and represented in a time–distance (T–D) plot. For all of the picked arrivals, the seismic profile geometry and shot information was then used for the inversion process of the seismic refraction tomography. The inversion was performed with Plotrefa software (SeisImager v12.2, Geometrics), where the initial model of the subsurface was created by providing a defined velocity range, dimensions, and a certain number of layers, which were converted to the gridded model of variable cell sizes. The cells were of constant velocity

and trace rays through the model. The iteration was set to a maximum value of ten for the Vp-model to reach the optimal RMS between the observed and calculated travel times [65].

The MASW method makes use of the dispersion characteristics of the surface waves recorded during seismic acquisitions. We applied the 1D MASW workflow (dispersion image, dispersion curve picking, editing, and inversion) in the Geometrics SeisImager/SW package (with recommended reference for the applied processing by [66]). The velocity structures derived from the active seismic measurements were obtained by using an inversion process based on the least squares approach. This aims at minimizing the RMS (root-mean-squared) between the observed dispersion curve and theoretical dispersion curves computed from the generated models. An initial model is given and modified after runs of iterations. The subsurface model that minimized the difference between the theoretical and observed dispersion curves was accepted as an approximate representation of the site.

### 3.3. UAV and DGPS Data Collection and Processing

The scarp region of the SAL on El Hierro (Figure 2) was investigated with a Mavic Pro UAV piloted with a controller connected to a mobile phone. On top of a high-quality camera/lens system, UAV photogrammetry usually requires stabilization during flights, dense image overlaps, and sufficient intersection angles. In this study, four manual flights were performed from different take-off sites at an elevation of about 320 m asl (above sea level) to collect 557 photos that were used to reconstruct a 3D surface model and a continuous ortho-mosaic image.

UAV-based photos were processed with Agisoft Metashape Professional software (v. 1.7.5). The first step consisted of discarding images with different views, inducing the whole set of images aligned improperly during the photo alignment. The numbers of projections and the error of the orientation expressed in pixels (i.e., pixel-error value) were used to identify misaligned photos within the set. Second, a dense point cloud (with 114,845 tie points) was created with an RMS reprojection error of 0.46–0.7 pixels based on the calculated exterior and interior image orientation parameters. This step also used the depth maps of overlapping image pairs to prepare multiple pairwise depth maps for each camera. These were merged into a joint depth map using excessive information in the overlapping regions to filter incorrect depth measurements. At this stage, the dense cloud still contained a lot of individual points (pixels) mostly related to the presence of vegetation, which had to be cleaned manually. As the light conditions changed during the image collection, the ‘calibrate colors’ option was used before the ‘build texture’ procedure and the creation of the continuous ortho-mosaic image. Finally, the digital elevation model (DEM) and the orthophotograph created from the dense cloud were exported with a ground resolution of 22 cm/pixel in a georeferenced raster format GeoTIFF). Both the orthoimage and the DEM are shown in Figure 3 (for this visualization, the DEM was downsampled to a 1 m resolution).

### 3.4. Rocks Characterization

Despite the abundant geological literature dedicated to El Hierro Island, laboratory or in situ descriptions of mechanical properties of rocks where the SAL developed are still missing. To fill this gap, we focused on rocks exposed in the water gallery behind the main SAL failure plane (Figure 2). These rocks most likely represent the geological conditions where the landslide main failure plane developed, providing a rare opportunity to directly observe them in more than a 900 m long exposure about 100 m to 400 m below the surface. These depths roughly correspond to the expected depths of the possible SAL sliding plane near its main scarp. Two intact samples of typical rocks from the gallery were extensively tested in the laboratory, while in situ, the geological strength index (GSI) [67] classification of lithologically distinct rock types, identified by [68], was performed inside the water gallery.

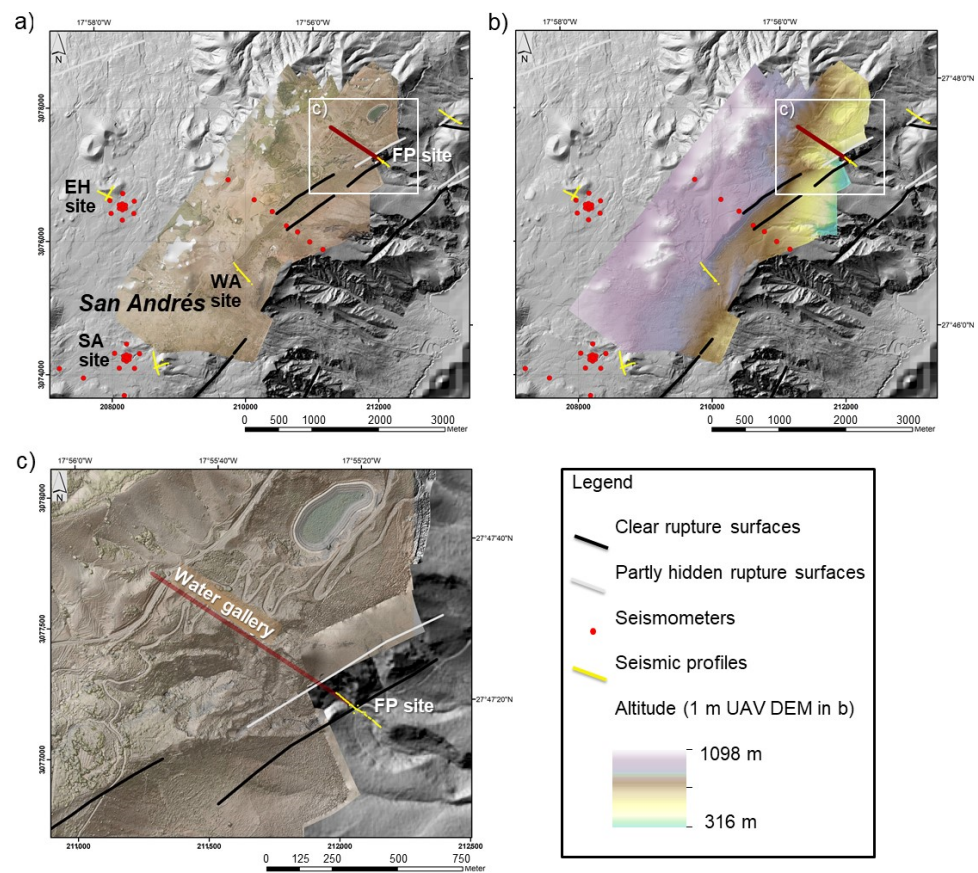


**Figure 3.** Results of the UAV surveys. (a) The 0.25 m resolution UAV imagery, (b) the derived 1 m DEM both overlaid on the 5 m LiDAR DEM hillshade. The inset (c) provides details of the area around the water gallery. EH—El Hierro, SA—San Andrés, IS—Isora, FP—Fault Plane, and WA—West Andres sites.

Petrography of the extracted basalt rocks samples (Figure S2) was described with the polarization microscope Leica DMR. All rock samples were also characterized by descriptive rock properties: density, porosity, and velocity of elastic waves. The mechanical behavior of the samples was then described by the determination of static and dynamic elastic moduli (cf., Young moduli, shear and bulk moduli, Poisson ratio), Brazilian tension strength, uniaxial strength, and triaxial strength at three levels of confinement. The dynamic elastic moduli were estimated from the velocities of seismic waves while the static ones were obtained from the stress–strain response of specimens loaded in uniaxial compression. All of the performed tests followed the standard ISRM test methods [69]. Equation (1) describes the general form of the Hoek–Brown failure envelope, where  $\sigma_1$  and  $\sigma_3$  are the major and minor effective principal stresses,  $\sigma_c$  is the uniaxial compressive strength of intact rock,  $m$ ,  $s$ , and  $a$  are the material constants ([70] and references therein).

$$\sigma_1 = \sigma_3 + \sigma_c \left( m \frac{\sigma_3}{\sigma_c} + s \right)^a \quad (1)$$

The obtained strengths at all conditions were approximated by the Hoek–Brown failure envelope (Equation (1), [71]) in a principal stresses space ( $\sigma_1$ ,  $\sigma_3$ ) by the Simplex method. As a result, we obtained the parameters  $m$  and  $\sigma_c$ , which characterize the intact rock ( $s = 1$  and  $a = 0.5$ ). Based on the GSI for rock mass and the expected residual GSI for the landslide itself, the Hoek–Brown envelopes for rock mass and its residual state were estimated [70,71].

### 3.5. Results Visualization and Interpretation

The newly acquired geophysical and geotechnical data at different scales and depths were interpreted using available topographic and geological information combined into the 3D models using Leapfrog Geo software by Seequent Ltd.© (version 2021.2). This software also allows for 3D data visualization in the complex morphological and geological context of the volcanic island edifice. The LiDAR (Light Detection and Ranging) DEM of the onshore portion of the island with sub-meter spatial resolution [57] was combined with the bathymetric data (isobaths of the ocean floor) [58] to prepare a continuous topographic surface. The previously published geological profiles [14] of the island were used for the preliminary geophysical data interpretation as one of the profiles closely followed the SEIS1 profile (Figure 2), while the other was situated across the Las Playas scarp area just SW from the SAL. This information, along with the geological map (1:25,000; [54]) and the field observations of the Las Playas escarpment, provide reliable independent information for the acquired geophysical data interpretations. The newly acquired onshore information enabled the modeling of the possible SAL sliding surface.

All data introduced into the model was first prepared on a GIS (geographic information system) platform. 1D and 2D data were inserted describing the geotechnical rock properties in the water gallery, or geological profiles and geophysical data interpretation (e.g., 1D thickness or velocity logs and 2D tomography profiles; see [72]).

## 4. Results

### 4.1. Results of the Geophysical Research

The UAV (unmanned aerial vehicle) survey provides detailed morphological and surface information of an area approximately of 10 km<sup>2</sup> surrounding the selected geophysical research sites and the water gallery (Figure 3). Such detailed aerial data depict all important surface features, whose interpretation can be related to the results of the shallow geophysical measurements. Comparison of the surface structural elements with known structural and lithological information from the water gallery [68] can be useful in assessing the weak slope sections relevant for future slope stability and deformation modeling.

#### 4.1.1. Active Seismic: SRT and MASW Results

The SRT profiles (Figure 4) displayed P-wave velocities ( $V_p$ ) from 320 to 2120 m/s, reaching a depth of approx. 40 m. Actually, higher values were also obtained along some profiles, but to be able to better compare the different SRT profiles, the scale was limited to 2120 m/s; we optimized this color-scale for all tomography sections; target  $V_p$ -value changes marking the presence of soft deposits and failure planes are typically less than 2000 m/s in these volcanic environments.

The EH1, EH2, SA1, and IS profiles were outside the SAL or in the case of the last two, they touched their suggested limit ([51], Figure 2). Due to their locations and limited depth reach, no specific characteristics related to the landslide mass could be derived. Nevertheless, the profiles EH1, EH2, and SA1 displayed a highly disturbed mass of tephra volcanic cones characterized by a low  $V_p$  near the surface. Most of these profiles displayed a high velocity of less disturbed rock environments at depths of about 35 m to 45 m.

The WA profile was located on the slope covered by the youngest basaltic lava flow (rift volcanism, Figure 2), which covered the extension trench below the main SAL failure plane [51] (Figure 4). Further to the SE (ca 450 m) from the profile end, the surface is disrupted by a series of scarps from where a deep-seated landslide block detached (see Figure 3 in [51]). Therefore, the region of increased  $V_p$  at the SE end of the WA profile probably reflects a less disturbed rock environment where the deep-seated landslide formed.

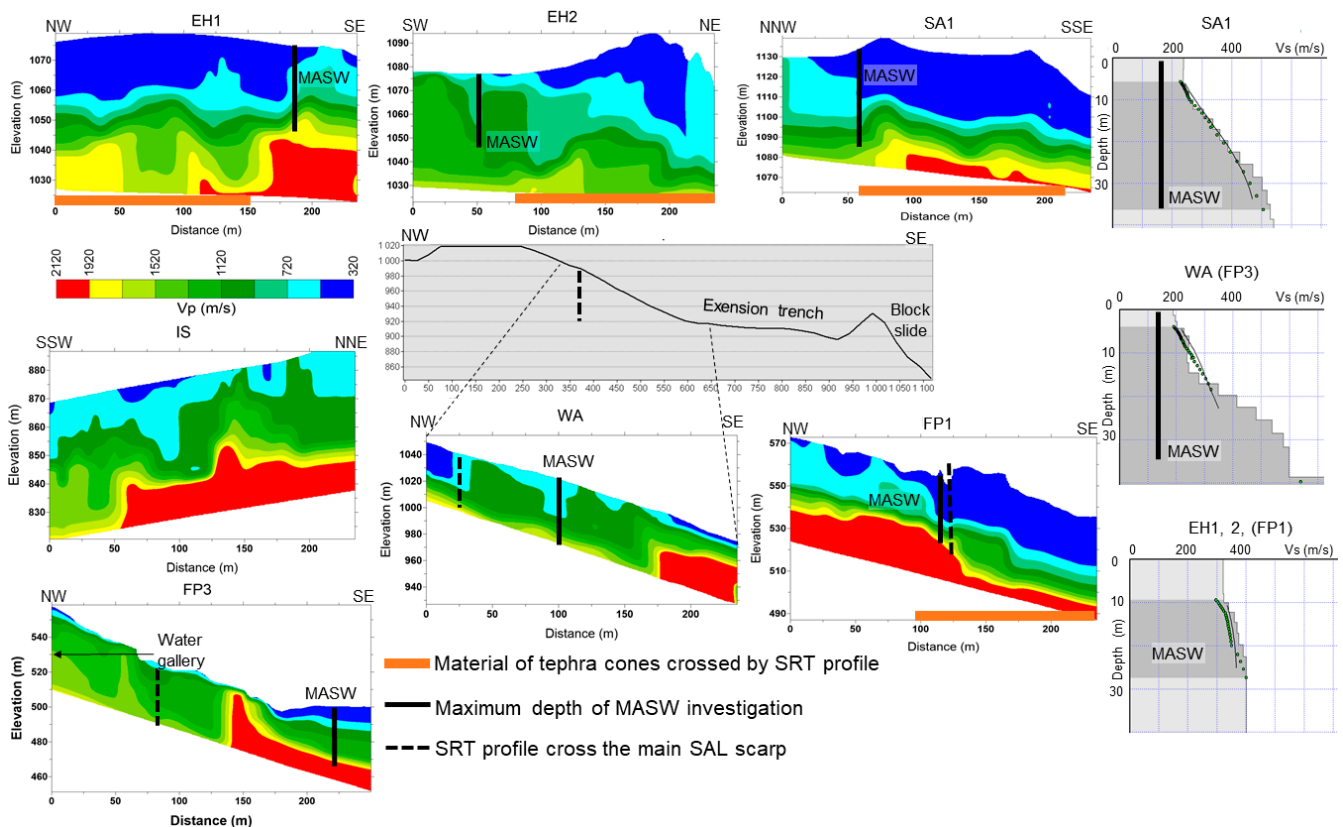


**Figure 4.** The SRT and MASW results (for location see Figure 2). The topographic profile in the center of the figure provides the geomorphological contexts for the WA profile.

The suggested failure plane of the SAL crossed by the FP1 profile corresponds to the vertical step in the high  $V_p$  area at the bottom of the profile. However, this vertical contrast in rock properties does not continue into the depth, and therefore, it is not possible to interpret it as the detachment plane of the deep-seated SAL. On the other hand, the very sharp contrast of  $V_p$  reflecting the known main failure plane of the SAL shows the FP3 profile. This profile suggests contrasting rock properties near the surface inside and outside the SAL main body. A low  $V_p$  near the surface at the SE end of the profile represents surface sediments accumulated within the ravine. The FP2 profile was not processed due to low data quality.

For all seismic profiles, the MASW analysis was also performed to obtain  $V_s$ -logs. Three representative  $V_s$ -logs are shown in Figure 5. They show that at all sites, the  $V_s$ -values of less than 600 m/s were measured down to a depth of 30 m. The lowest  $V_s$ -values of less than 300 m/s near the surface were obtained for the SA and WA, and even lower for FP3 sites, typically where the profiles crossed the SAL scarp.

#### 4.1.2. Passive Seismic: Array and H/V Results

Results of the ambient noise measurements are shown in terms of the phase velocity dispersion curve and the related  $V_s$ -log obtained by the inversion of the respective dispersion curve (Figure 5). The results obtained for the EH and SA arrays located outside the SAL landslide on the flat region on both sides of the main rift zone were quite similar. The  $V_s$ -log detected the first velocity increase from 400 to 1000 m/s at a depth of about 30–40 m and a second increase to 1500 m/s (SA array) and 1800 m/s (EH array) at a depth of about 240 m. The shallow depth of the  $V_s$  increase agreed with the SRT results at the respective sites (Figure 4). Data obtained from the IS site inside the suggested limits of the SAL document velocity increased at three depths, largely different from the previous sites. The first increase of  $V_s$  from 250 m/s to 700 m/s appeared at the depth of 30 m,

followed by a  $V_s$  increase to 1000 m/s at a depth of 80 m. The most distinct increase of  $V_s$  to about 2200 m/s could be observed at a depth below 420 m. Velocities measured between depths of 80 m and 420 m within the SAL were similar to the velocities obtained for the depths between 40 m and 240 m on sites outside the SAL (cf., SA, EH). The lower near-surface  $V_s$  reaching greater depths within the landslide indicates a more intense and deeper disintegration of rocks within the unstable part.

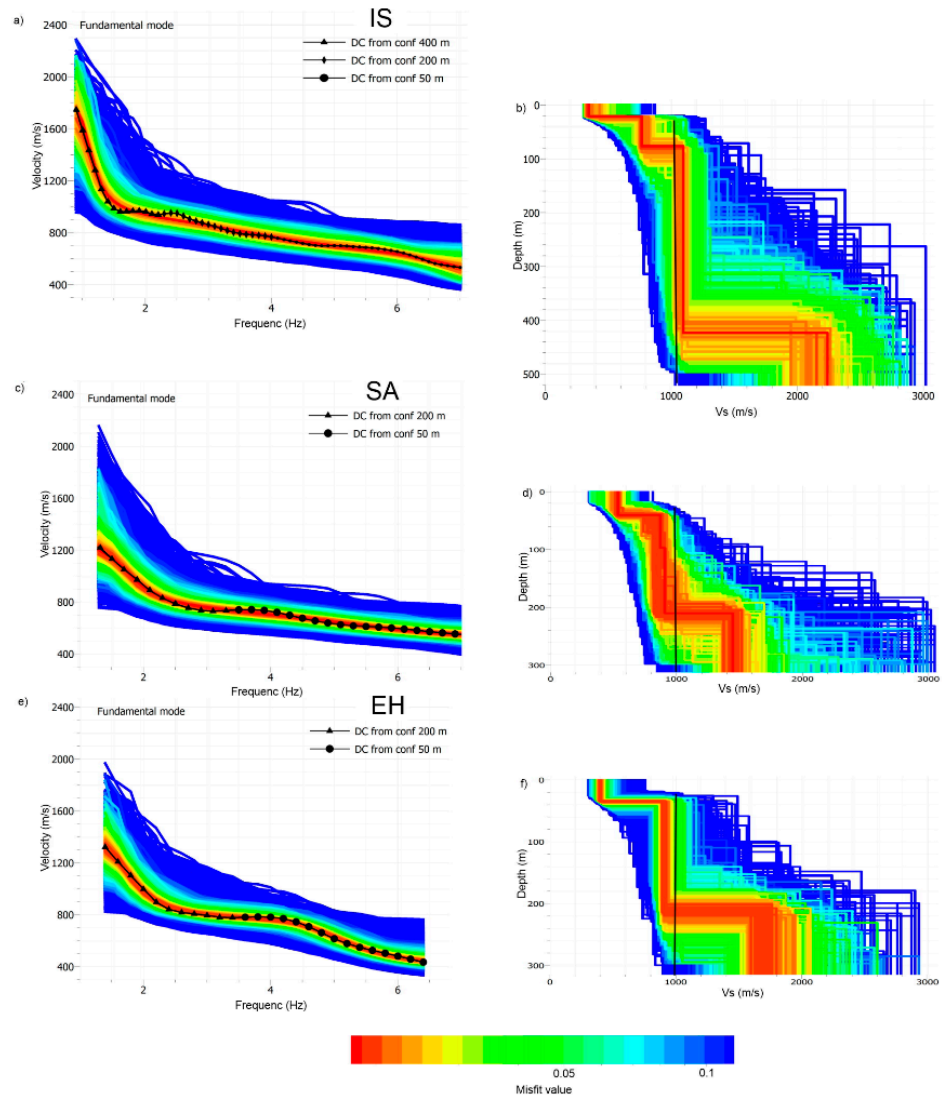


**Figure 5.** Phase velocity dispersion curves (a,c,e) and the derived shear wave velocity structures (b,d,f) obtained by the inversion of vertical component ambient noise arrays installed at the IS, SA, and EH sites (locations are in Figure 2).

As indicated above, all station recordings within the arrays were also used for H/V analysis (i.e., the determination of the fundamental frequency of the recorded ambient noise). Related results were then transformed into depth-logs for the near-surface lower  $V_s$  layer. For the latter, we considered an average of  $V_s = 900$  m/s (averaging the  $V_s = 400$ – $700$  m/s for the first 30–90 m and the  $V_s$  of 1000 m/s for the second–third layer above the deepest contrast—see an increase of  $V_s$  in the lowest part of the logs). Additionally, all seven stations had been installed during one day along two different profiles, SEIS1 and SEIS2. In total, 45 (EH = 13, SA = 13, IS = 18) ambient noise H/V logs were obtained for the arrays and 13 for the two profiles.

The detailed analysis of ambient noise recordings along the SEIS1 profile show a very clear peak at 0.7–1 Hz ( $f_0$ ) for all stations. The fundamental frequencies  $f_0$  slightly decreased

toward the east at recording stations located within the SAL (Figure 6). Above the main SAL scarp, the upper stations were also marked by a second peak at a frequency  $f_1$  of 3–4 Hz. Along the profile SEIS2, the data present a fundamental peak below 1 Hz only for stations within the SAL. Some of these stations also recorded the second peak with  $f_1 = 4.5$  Hz. The peak at a lower frequency ( $f_0$ ) for the stations located above the main failure plane at the SEIS2 profile was about 5 Hz. The H/V analysis showed a clear difference between the maximum depth of the near-surface velocity contrast outside and inside the SAL for the SEIS2 profile only.

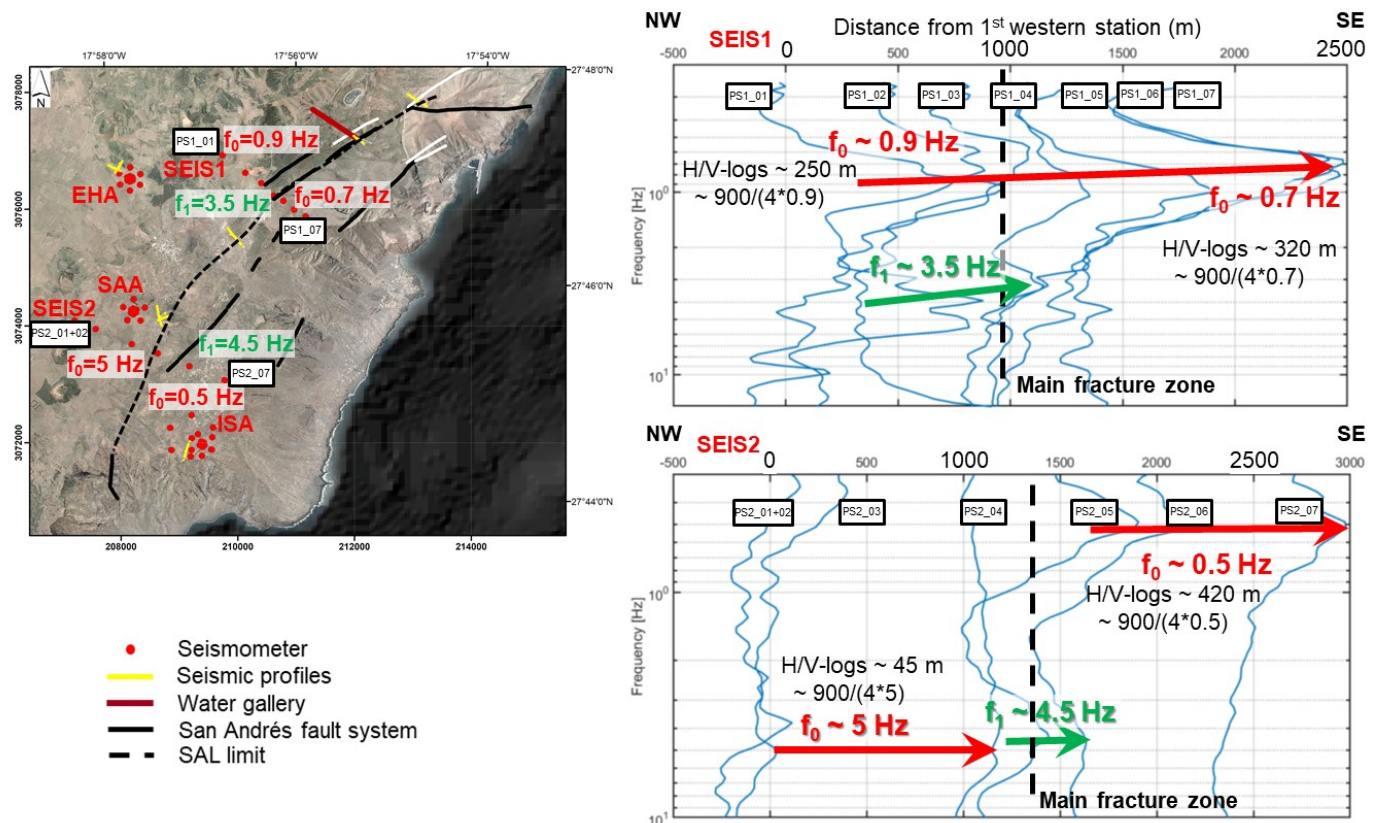


**Figure 6.** Analysis (H/V ratios) of the ambient noise recordings along the two seismological profiles (SEIS1, SEIS2) with interpretation in terms of fundamental ( $f_0$ ) and higher, second ( $f_1$ ) resonance peak frequencies.

If we consider the aforementioned average  $-V_s$  of 900 m/s for the entire near-surface layer above the deepest  $V_s$ -contrast (Figure 6), the latter would then have a thickness of about 250 m in the upper part ( $f_0 = 0.9$  Hz) of the SEIS1 profile and of 320 m ( $f_0 = 0.7$  Hz) in the lower part. In the SEIS2 profile, this layer had a much smaller thickness of 45 m ( $f_0 = 5$  Hz), while it was probably considerably thicker within the SAL at 420 m ( $f_0 = 0.5$  Hz), with a clear change between the third and fourth stations located on either side of the main rupture plane, likely to be related to the increased thickness of weaker rocks.

#### 4.2. Laboratory and In-Situ Rock Properties Description

The two characteristic rocks from the water gallery were macroscopically different with one containing a significant amount of macropores, while the other had a highly compact appearance. The petrographic analysis confirmed the distinct character of the rocks. The latter (further referred to as compact basalt) was a homogenous, fine-grained basalt containing relatively rare phenocrysts of olivine (Table 1). Its groundmass contains predominantly plagioclase and pyroxene, having an ophitic texture without indications of preferred fabric orientation (Figure S3a). The second sample (further referred to as porous basalt) was highly heterogenous, distinctly porous basaltic rock. It contained a

relatively high amount of olivine phenocrysts (with a high level of alteration and microcrack density) together with relatively bigger particles of volcanic glass and a very high number of spherical pores. This rock most likely represents part of the volcanic slags from the upper part of the lava flow, formed possibly in the underwater environment (Figure S3b).

**Table 1.** Basic petrographic characteristics of the tested rock estimated from the microscopic photographs.

Rock Constituent	Compact Basalt			Porous Basalt		
	Content [%]	Grain size [mm]	Description	Content [%]	Grain Size [mm]	Description
Groundmass (plagioclase, pyroxene)	80–90%	<0.1	No preferential orientation, alteration, microcracks	30–50%	<0.3	No preferential orientation, alteration, microcracks
Olivine fenocrysts	5–10%	0.5–1	No preferential orientation, and alteration, low microcrack density	20–30%	1–1.5	No preferential orientation, medium alteration, high microcrack density
Volcanic glass	0%	-	-	10–20%	0.3–1.5	No preferential orientation, alteration, microcracks
Macropores	<1%	0.1–0.3	Ellipsoidal shape without preferential orientation	2–5%	0.2–1	Ellipsoidal shape without preferential orientation

The descriptive properties of both basalts (Table 2) showed a very similar density of the mineral matrix, while the decreased velocity of seismic waves for the porous basalt indicated a one-order higher porosity compared to the compact basalt. The shear wave velocities were about 20% higher from the lab experiments than their equivalents obtained from the in situ geophysics for the rock basement. This difference is related to the scale effect in the sample size as well as in the wavelengths of both approaches.

**Table 2.** Descriptive properties of the tested basalts: dried density ( $\rho_{d\_AV}$ ), specific gravity ( $\rho_s$ ), porosity (n), P wave velocity ( $V_P$ ), shear wave velocity ( $V_S$ ). mean—average value, N—number of tests, std—standard deviation.

Rocks		$\rho_{d\_AV}$ [g/cm <sup>3</sup> ]	$\rho_s$ [g/cm <sup>3</sup> ]	n [%]	$V_P$ [m/s]	$V_S$ [m/s]
Compact basalt	mean	2.931	2.942	0.367	5768	3347
	N	5	3	5	5	5
	std	0.004	0.003	0.144	0.083	0.065
Porous basalt	mean	2.836	2.929	3.176	4647	2836
	N	3	3	3	3	3
	std	0.034	0.005	1.175	0.070	0.034

For both rocks, the dynamic moduli were about 25% higher than the static ones (Table 3), which is a known effect related to the different sensitivities of both methods to the rock microstructure [73]. Interestingly, both basalts displayed a practically equal dynamic and static Poisson ratio. Porous basalt displayed about 40% lower values of elastic constants (E,  $\nu$ , K) and a distinctly higher Poisson ratio. Considering the basalts, [74] reported very similar, porosity-related elastic behavior.

**Table 3.** Dynamic and static elastic moduli. E—Young moduli,  $\nu$ —Poisson ratio,  $\mu$ —shear moduli, K—bulk moduli.

Rocks	Elastic Moduli	E [GPa]	$\nu$	$\mu$ [GPa]	K [GPa]
Porous basalt	DYNAMIC	46.0	0.20	19.1	25.8
	STATIC	36.4	0.21	15.0	21.0
Compact basalt	DYNAMIC	81.9	0.25	32.9	53.8
	STATIC	59.8	0.25	24.0	39.7

The estimated strengths, under various loading conditions, are listed in Table 4. The tension strength was similar for both rocks. Nevertheless, under uniaxial or confined compression, the porous basalt was significantly weaker (100–200%).

**Table 4.** Measured strengths for both the tested basalts (bold numbers) and corresponding principal stresses at the failure for particular tests. BTS—Brazilian tension strength, DTS—estimation of direct tension strength  $\sim 0.9 \cdot \text{BTS}$  [75], UCS—uniaxial compressive strength, TCS—triaxial compressive strength.

Rocks	Principle Stress	BTS [MPa]	DTS [MPa]	UCS [MPa]	TCS [MPa]		
Porous basalt	$\sigma_1$	<b>−10.2</b>	<b>−9.2</b>	0.0	7.0	15.0	25.0
	$\sigma_1$	-	0.0	<b>86.5</b>	<b>150.7</b>	<b>179.5</b>	<b>207.9</b>
Compact basalt	$\sigma_3$	<b>−11.4</b>	<b>−10.3</b>	0.0	7.0	15.0	30.0
	$\sigma_1$	-	0.0	<b>343.9</b>	<b>411.5</b>	<b>441.1</b>	<b>554.6</b>

The parameters for the Hoek–Brown failure envelopes are listed in Table 5. For the intact rock, the compact basalt with  $m = 27.6$  (Table 5) was in the mid-range typical for basalts [76]. On the other hand, the  $m = 10.6$  (Table 5) of porous basalt was much lower than expected and the rock displayed a significantly different mechanical behavior. These differences were possibly due to the high porosity and high content of volcanic glass for the porous basalt.

**Table 5.** Parameters of the Hoek–Brown failure envelope ( $s$ ,  $m$ ,  $a$ ) for the intact rock, rock mass, and residual state.

Rock Type	Rock State	GSI [-]	$s$ [-]	$m$ [-]	$a$ [-]	UCS [MPa]	DTS [MPa]
Basalt Porous	Intact	100.0	1.000	10.636	0.500	98.700	9.20
	Rock mass	80.0	0.108	5.207	0.501	32.436	2.90
	Residual	40.0	0.001	1.300	0.511	3.121	0.45
Basalt Compact	Intact	100.0	1.000	27.574	0.500	284.600	10.00
	Rock mass	80.0	0.108	13.499	0.501	93.529	2.30
	Residual	40.0	0.001	3.235	0.511	9.000	0.24

Based on the in situ examination of the water gallery, the GSI of the rock mass was estimated to vary from 45 to 70. A rather large GSI index spread reflects the contrasting rock properties of varying lithologies. The highest index values of good quality rocks (GSI 55 to 70) characterize lava flows (e.g., apatite or olivine, [68]). Rocks classified as fair (45 to 55) represent mainly highly disintegrated dykes. Large portions of the gallery walls are built by scoria or welded pyroclasts [68], whose character is closer to soils than to fractured rocks, thus the GSI is not appropriate to estimate their strength properties [77]. Rocks documented in the water gallery represent gravitationally non-disturbed rocks outside the main SAL landslide body. Thus, we can consider them to be representative of conditions

before the SAL occurrence near its scarp. The estimated GSI range (45–70) was used to obtain the Hoek–Brown envelopes for rock mass [71]. The expected GSI range (20–35) for the residual state [70] was used to obtain the Hoek–Brown envelopes characterizing the landslide itself (Table 5, Figure S4). The microstructure influence on the strength decreased with the GSI, resulting in a similar behavior at the residual state for both the examined basalts (Table 5).

#### 4.3. Geological Modeling

Available data allowed for the preparation of models at different scales covering the entire Canary Islands or to show a complete central geological cross-section [14] of the El Hierro Island (Figure 7a) to a detailed view with the Vs structure for the EH site (Figure 7b). Visualization of the geophysical data interpretation along with the geological cross-section suggests that the Vs increase at the depth of about 240 m may be related to the sequence of more recent lava flows (Figure 7b). An overview of the Vs- and HV-logs well illustrates the position of the contrasting rock properties, which is deeper inside the SAL limits, where it could indicate the location of a planar sliding surface (c, d in Figure 7, 320 m and 420 m depths of the SEIS1 and SEIS2 profiles and the IS site).

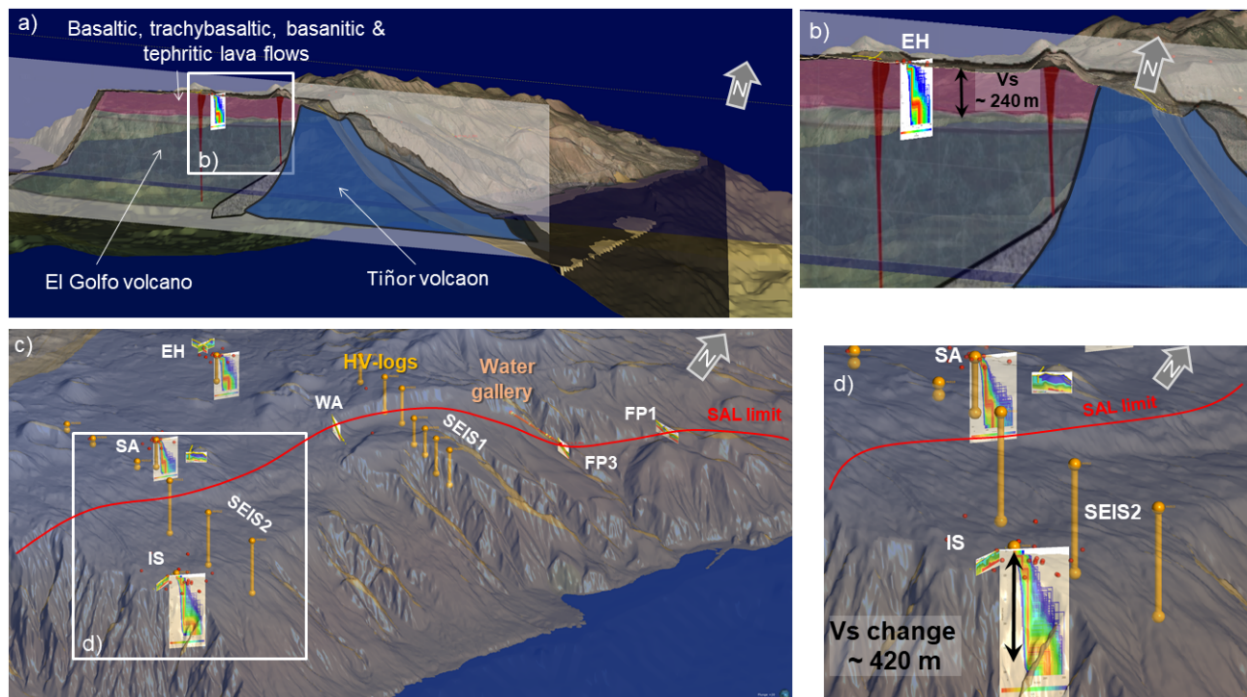


**Figure 7.** 3D geomodel of the studied El Hierro. (a) The central part of the SAL with inserted geological cross-section and geophysical results with the detailed view in the inset (b); (c) view of the SW part of the San Andrés landslide with the results of the geophysical measurements and detailed view in the inset (d).

All the above show the information that was used to compute a possible sliding surface of the SAL. The onshore part of the sliding surface was extrapolated by using the geophysical data and by extending the so-formed sliding surface until the crossing of the slope in the submarine part. The related raster surface was prepared by the Kriging algorithm in ArcMap 10.8 and the result was combined with the 50 m resolution DEM. This failure surface model was imported into the geomodel as a point cloud and re-interpolated as a surface (Figure 8).

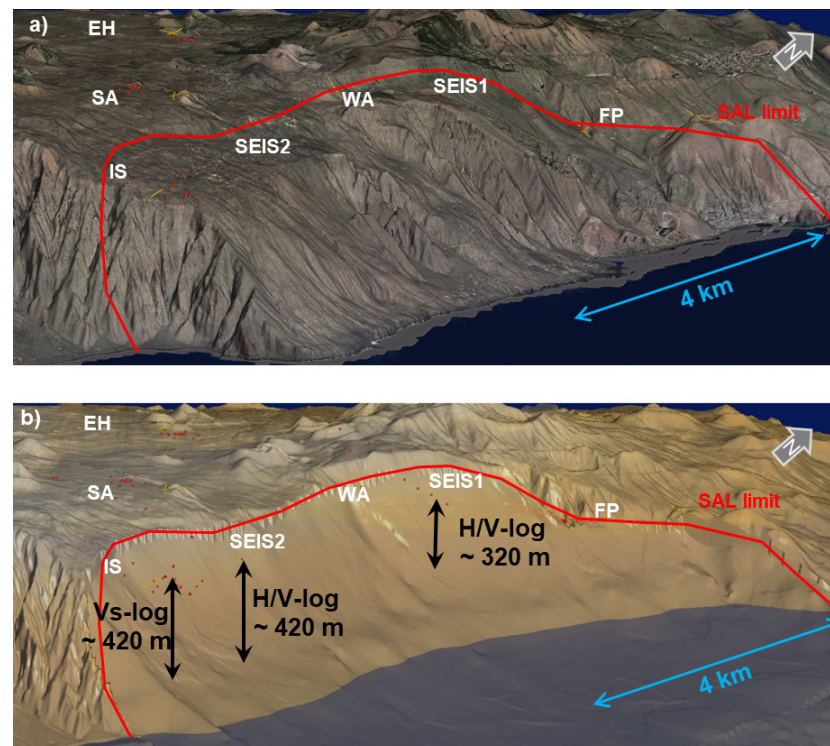


**Figure 8.** Oblique views (from SE) of the 3D geomodel of the San Andrés landslide. (a) A recent topography with a 0.25 m orthophoto (source [78]); (b) the possible sliding surface inferred from the geophysical data analysis (the 20 m DEM-bathymetry with a semi-transparent ocean surface is also shown). The locations of the geophysical field measurement sites are indicated.

## 5. Discussion

Gravitational slope movements usually change the properties of the transported material. Nevertheless, our results of the ambient noise array measurements suggest that rocks outside and within the SAL have very similar seismic properties considering  $V_s$  above the 240 m and 420 m impedance contrasts. The detected differences (cf., 1050 m/s inside and 900 m/s outside the SAL limits) were too small to be related to different rock properties. This finding is in contrast to the results commonly obtained from deep-seated landslides in which displaced rocks usually show clear signs of deterioration compared with rocks outside their limits (e.g., [78]). This suggests a low internal disruption of the rock material during the SAL movement, which was very fast and localized on the main sliding plane [6]. Cases of fast-moving landslides transporting considerable volumes of rock without significant internal disruption are rare and related to earthquakes (e.g., Tsaoling landslide, Taiwan, [79]). Differences in the rock composition outside and inside the SAL were observed on the H/V ratios of the ambient noise recordings, showing the maximum depth of the near-surface low  $V_s$  layer (<1000 m/s, Figure 6). This layer had a greater thickness within the SAL (cf., 320 m on SEIS1, 420 m on SEIS2) than outside (cf., 250 m on SEIS1, 45 m on SEIS2, Figures 6 and 7).

The geophysical research also aimed to find and describe the possible sliding surface of the SAL and to observe the expression of the SAL main scarp in the data. The main scarp was not captured on the profiles of WA and FP1 while the profiles of SEIS1,2 and FP3 showed it clearly. This is evidenced by the increase in the maximum depth of the near-surface low  $V_s$  layer (<1000 m/s, Figure 6) when crossing the scarp to the SAL; on the FP3 profile, this is marked by the locally increasing depth of the rocks marked by  $V_p < 720$  m/s (Figure 4). The surface parallel 420 m impedance contrast identified on the IS site array and the ambient noise recordings along the SEIS2 profile were considered as the possible planar or slightly curved sliding plane of the SAL. Similarly, we interpreted

the SEIS1 results with the depth of possible sliding surface at 320 m. Our findings roughly correspond to the hypothesized SAL sliding surface in [47]. Despite this, the existence of deeper sliding surfaces beyond the reach of the geophysical measurements cannot be ruled out. The non-uniform expression of the main scarp in the geophysical data (as well as the surface morphology) [51] and different depths of the possible SAL sliding planes illustrate the lateral change (e.g., in NE–SW direction) in the internal structure of the SAL. This might have been caused by the partition of the SAL into separate blocks identified and described in the previous research using morphological evidence [29,51].

The detailed petrographic description and mechanical characterization of two samples of basalt rocks extracted from the water gallery showed the high variability in their strength properties (cf., compression strength, elastic moduli, Tables 3 and 4) caused by the contrasting porosity of the rocks. Concerning the properties of the bulk rock material outside as well as inside the SAL, these samples represent the most competent members of the geological environment. The GSI rock mass characterization inside the 900 m long water gallery provided a complex description of the bulk rock properties, evidencing their high variability, which is characterized by sharp lithological contrasts. This, along with fractures and discontinuities, form the bulk rock characteristics also reflected on a large scale in the geophysical measurements. Combining these data, a comparison of the in situ observations with the results of the geophysical measurements is possible. The impedance contrast at the 250 m depth identified on the SEIS1 profile outside the SAL limits (Figure S5) cuts halfway across the gallery. This is roughly in the place where the detailed geological mapping [68] identified olivine lava flows of good quality (GSI 55 to 70). Although this comparison suggests a straightforward link between the in situ rocks and geophysical data processing results, it is important to consider several drawbacks that may hamper such a direct linkage. The geophysical contrast at the site of the water gallery was extrapolated from the SEIS1 profile and may not represent the actual conditions inside the water gallery located 1.7 km to the NE. At the same time, the rock properties are in contrast to the results from the inversion processes, which provide the averaged mechanical properties within large rock volumes.

Although the geophysical research results do not provide evidence about the degradation of rock properties within the SAL limits, we applied the approach from [70] to estimate the degradation of the observed GSI values to their residual levels (Figure S4). The GSI values obtained from direct estimation in the water gallery and their residual values were used to obtain Hoek–Brown envelopes for the rock mass and its residual state. For the rock mass or residual state, all material parameters in Equation (1) ( $m$ ,  $s$ , and  $a$ ) are functions of GSI and can be obtained by the degradation of the corresponding values for intact rock (Equations (15)–(17) in [70]). In the case of rock mass, we used both extreme values of GSI: 70 (massive brittle rock) and 45 (jointed intermediate rock). Similarly to [70], we used the GSI for the residual state of massive brittle rock (GSI = 35) and jointed intermediate rock (GSI = 20). The obtained parameters for all of the envelopes (Figure S4) are shown in Table 5 where UCS and DTS [75] are estimations of the uniaxial compression and uniaxial tension strengths, respectively, based on the intersection of the Hoek–Brown envelopes and the  $\sigma_1$  and  $\sigma_3$  axis (Figure S4). As expected, both basalt types showed significantly different failure envelopes for the rock mass and residual state, respectively. It is worth mentioning that the range in the residual envelopes based on the rock mass state is rather small.

The newly acquired information about the inner structure and rock properties of the SAL was largely based on indirect (cf., geophysical) observations with a significant, but still limited depth reach, where identified contrasts in the rock environment resulted from inversion processes based on the characterization of the bulk rock properties. At the same time, the interpretation of the results is at least partly shaped by previous knowledge. While this does not diminish the benefits of the research conducted, further investigations should focus on refining the results obtained. Therefore, the existence of deeper sliding surfaces beyond the reach of the geophysical measurements and the presence of the suggested SAL sliding planes needs to be confirmed through an independent method. The newly obtained

rock mechanical properties describing intact rocks, rock masses, and their residual states can be used to define credible boundary conditions for numerical slope deformation or stability modeling (e.g., [80]), which have proven to be useful in revealing deep-seated landslide dynamics.

## 6. Conclusions

The performed complex geological and geophysical research of the San Andrés mega-landslide revealed new details about its internal structure and the volcanic rock properties outside and inside its on-shore limits. The geophysical data also proved to be capable of identifying the main SAL scarp in areas covered by younger lava flows (e.g., in the SW part of the SAL). These illustrate the change in the rock properties from the surface toward the depth described by the changing S- and P-wave velocities obtained by combining ambient noise recordings with active seismic prospecting. Several significant contrasts were identified near the surface where rocks were more fractured (down to 45 m), followed by a more competent material above the largest shear wave velocity contrast (cf., increase from 1000 m/s to 2200 m/s) at a depth of up to 420 m. The deepest related contrast was measured in the SW part of the SAL, while it was a bit shallower (depth of 320 m) in the NE part; these values most probably indicate the depth of a planar (or slightly curved), roughly surface-parallel SAL sliding plane. Although the existence of deeper planes cannot be ruled out, newly obtained geophysical evidence about a possible SAL sliding plane is an important step toward a better understanding of the recent stability conditions of the landslide. Similar rock properties found inside and outside the SAL suggest that its previous catastrophically fast movement did not affect the bulk properties of the transported rocks as it chiefly occurred along the weakened plane forming the main SAL scarp (also termed as the San Andrés fault). Nevertheless, the strength properties of the rocks examined by geophysical methods varied significantly, even across relatively short distances (e.g., several hundreds of meters), as shown by the performed laboratory and in situ geotechnical analysis. The geological strength index determined in the 900 m long water gallery revealed good to very poor-quality rocks chaotically distributed along its course. Samples of two basalt rocks from the same gallery exhibited similar tension strengths. The rock that probably formed in the underwater environment was significantly weaker (100–200%) under uniaxial or confined compression; this can be largely explained by its one-order higher porosity compared to the other basalt rock.

The collected data also included high spatial resolution (cf., 0.25 m) UAV imagery that were integrated within the 3D geological model to enhance their visual interpretation and to form the basis for the preparation of a representative geotechnical model. Such a model will be used to compute the slope stability and simulate slope deformation over the San Andrés landslide, accommodating the inherent uncertainties by defining multiple failure scenarios. This would further contribute to a better hazard assessment of the landslides on volcanic islands, which are among the largest known mass movements on Earth.

**Supplementary Materials:** The following supporting information can be downloaded at: <https://www.mdpi.com/article/10.3390/rs15061627/s1>, Figure S1: Four examples of the H/V curves indicating prominent subsurface contrasts. The identified resonance frequencies are marked with gray solid lines and the values along with the location identifiers are in the titles; Figure S2: Photograph (c) shows an extraction of the rock sample of the porous basalt (for explanation see text); Figure S3: Photographs from the polarization microscope Leica DMR: (a) compact basalt, (b) porous basalt. The photographs show clear microstructure differences of the two tested types of basalts (Ol—olivine, Pl—plagioclase, Po—pores, Gl—volcanic glass); Figure S4: Hoek-Brown failure envelopes for intact rock, rock mass and residual rock mass for compact (a) and porous (b) basalts. The values of measured strengths of intact rock are in Table 4, while the parameters of all envelopes are in Table 5; Figure S5: 3D view showing the spatial relationship of the water gallery and impedance contrast identified from the SEIS1 profile measurements.

**Author Contributions:** Conceptualization, H.-B.H. and J.K.; Methodology, formal analysis, and validation, H.-B.H., Y.H., L.C. and M.P.; Investigation, M.P., J.B., M.R., H.-B.H., L.C., R.S., V.P., A.-S.M., Y.H., S.M. and J.K.; Writing—original draft preparation, H.-B.H., J.K. and J.B.; Writing—review and editing, H.-B.H., A.-S.M., L.C. and Y.H.; Visualization, H.-B.H. All authors have read and agreed to the published version of the manuscript.

**Funding:** Article preparation was supported by the Mobility Plus project of the Czech Academy of Sciences and F.R.S.-FNRS, Belgium no. FNRS-20-01 “Investigation, Monitoring, and Modeling of the Eastern incipient Flank Collapse of El Hierro volcano, Canary Islands”. Investigations of M.P. were supported by the Czech Academy of Sciences project no. RVO 67985831.

**Data Availability Statement:** The data presented in this study are available on request from H.-B.H. The data are not publicly available due to further processing for upcoming publications.

**Acknowledgments:** We thank Michal Kusák, Emilie Lemaire, Camille Baudinet, Marine Julémont, Valmy Dorival, Vipin Kumar, Philippe Cerfontaine, and the personnel of the Centro Geofísico de Canarias (IGN) for their support during the field geophysical measurements.

**Conflicts of Interest:** The authors declare no conflict of interest.

## References

1. Masson, D.G.; Le Bas, T.; Grevemeyer, I.; Weinrebe, W. Flank collapse and large-scale landsliding in the Cape Verde Islands, off West African. *Geochem. Geophys. Geosyst.* **2008**, *9*, Q07015. [[CrossRef](#)]
2. Blahút, J.; Balek, J.; Klimeš, J.; Rowberry, M.; Kusák, M.; Kalina, J. A comprehensive global database of giant landslides on volcanic islands. *Landslides* **2019**, *16*, 2045–2052. [[CrossRef](#)]
3. Hunt, J.E.; Wynn, R.B.; Talling, P.J.; Masson, D.G. Multistage collapse of eight western Canary Island landslides in the last 1.5 Ma: Sedimentological and geochemical evidence from subunits in submarine flow deposits. *Geochem. Geophys. Geosyst.* **2013**, *14*, 2159–2181. [[CrossRef](#)]
4. Hunt, J.E.; Jarvis, I. Prodigious submarine landslides during the inception and early growth of volcanic islands. *Nat. Commun.* **2017**, *8*, 2061. [[CrossRef](#)]
5. León, R.; Somoza, L.; Urgeles, R.; Medialdea, T.; Ferrer, M.; Biain, A.; García-Crespo, J.; Mediato, J.; Galindo, I.; Yepes, J.; et al. Multi-event oceanic island landslides: New onshore-offshore insights from El Hierro Island, Canary Archipelago. *Mar. Geol.* **2017**, *393*, 156–175. [[CrossRef](#)]
6. Blahút, J.; Mitrovic-Woodell, I.; Baroň, I.; René, M.; Rowberry, M.; Blard, P.-H.; Hartvich, F.; Balek, J.; Meletlidis, S. Volcanic edifice slip events recorded on the fault plane of the San Andrés Landslide, El Hierro, Canary Islands. *Tectonophysics* **2020**, *776*, 228317. [[CrossRef](#)]
7. Bernard, B.; Takarada, S.; Andrade, S.D.; Dufresne, A. Terminology and Strategy to Describe Large Volcanic Landslides and Debris Avalanches. In *Volcanic Debris Avalanches: From Collapse to Hazard*; Roverato, M., Dufresne, A., Procter, J., Eds.; Springer: Cham, Switzerland, 2021; pp. 51–73. [[CrossRef](#)]
8. Owen, S.E.; Bürgmann, R. An increment of volcano collapse: Kinematics of the 1975 Kalapana, Hawaii, earthquake. *J. Volcanol. Geother. Res.* **2006**, *150*, 163–185. [[CrossRef](#)]
9. Blahút, J.; Klimeš, J. Causes and triggers of mass-movements: Volcanic activity. In *Treatise on Geomorphology*; Elsevier: Amsterdam, The Netherlands, 2021. [[CrossRef](#)]
10. Day, S.; Carracedo, J.-C.; Guillou, H. Age and geometry of an aborted rift flank collapse: The San Andres fault system, El Hierro, Canary Islands. *Geol. Mag.* **1997**, *134*, 523–537. [[CrossRef](#)]
11. Jongmans, D.; Garambois, S. Geophysical investigation of landslides: A review. *Bullet. Société Géologique Fr.* **2007**, *178*, 101–112. [[CrossRef](#)]
12. Panzera, F.; Lombardo, G.; Monaco, C. New evidence of wavefield polarization on fault zone in the lower NE slope of Mt. Etna. *It. J. Geosci.* **2016**, *135*, 250–260. [[CrossRef](#)]
13. Hussain, Y.; Schlögel, R.; Innocenti, A.; Hamza, O.; Iannucci, R.; Martino, S.; Havenith, H.-B. Review on the Geophysical and UAV-Based Methods Applied to Landslides. *Remote Sens.* **2022**, *14*, 4564. [[CrossRef](#)]
14. Carracedo, J.-C.; Rodríguez Badiola, E.; Guillou, H.; De la Nuez, H.; Pérez Torrado, F. Geology and volcanology of the western Canaries: La Palma and El Hierro. *Estud. Geol.* **2001**, *57*, 171–295.
15. Delgado, J.; Galiana-Merino, J.J.; García-Tortosa, F.J.; Garrido, J.; Lenti, L.; Martino, S.; Soler-Earle, P.S.; Shearer, P.M. Characterization of global seismograms using an automatic-picking algorithm. *Bull. Seism. Soc. Am.* **1994**, *84*, 366–376.
16. Ryberg, T.; Kirsch, M.; Haberland, C.; Tolosana-Delgado, R.; Viezzoli, A.; Gloaguen, R. Ambient seismic noise analysis of LARGE-N data for mineral exploration in the Central Erzgebirge, Germany. *Solid Earth* **2022**, *13*, 519–533. [[CrossRef](#)]
17. Jornet-Monteverde, J.A.; Galiana-Merino, J.J.; Soler-Llorens, J.L. Design and implementation of a wireless recorder system for seismic noise array measurements. *Sensors* **2022**, *22*, 8103. [[CrossRef](#)] [[PubMed](#)]
18. Hussain, Y.; Cardenas-Soto, M.; Martino, S.; Moreira, C.; Borges, W.; Hamza, O.; Martinez-Carvajal, H. Multiple geophysical techniques for investigation and monitoring of Sobradinho landslide, Brazil. *Sustainability* **2019**, *11*, 6672. [[CrossRef](#)]

19. Mreyen, A.-S.; Cauchie, L.; Micu, M.; Onaca, A.; Havenith, H.-B. Multiple geophysical investigation to characterize massive slope failure deposits: Application to the Balta rockslide, Carpathians. *Geoph. J. Int.* **2021**, *225*, 1032–1047. [[CrossRef](#)]
20. Calamita, G.; Serlenga, V.; Stabile, T.A.; Gallipoli, M.R.; Bellanova, J.; Bonano, M.; Perrone, A. An integrated geophysical approach for urban underground characterization: The Avigliano town (southern Italy) case study. *Geomat. Nat. Haz. Risk* **2019**, *10*, 412–432. [[CrossRef](#)]
21. Chatzis, N.; Papazachos, C.; Theodoulidis, N.; Hatzidimitriou, P.; Vougioukalakis, G.; Paulatto, M.; Heath, B.; Hooft, E.; Toomey, D.; Anthymidis, M.; et al. Metamorphic bedrock geometry of Santorini using HVSR information and geophysical modeling of ambient noise and active-source surface-wave data. *J. Volcan. Geotherm. Res.* **2022**, *432*, 107692. [[CrossRef](#)]
22. Natali, M.; Lidal, E.M.; Parulek, J.; Viola, I.; Patel, D. Modeling terrains and subsurface geology. In *Eurographics 2013—State of the Art Reports*; The Eurographics Association: Eindhoven, The Netherlands, 2013; pp. 155–173. [[CrossRef](#)]
23. Caumon, G.; Collon-Drouaillet, P.; De Veslud, C.L.C.; Viseur, S.; Sausse, J. Surface based 3D modeling of geological structures. *Math. Geosci.* **2009**, *41*, 927–945. [[CrossRef](#)]
24. Lerch, C.; Hoppe, A. Development of a geological 3D-model for improved calculations of groundwater vulnerability. *Grundwasser* **2007**, *12*, 144–153. [[CrossRef](#)]
25. Havenith, H.-B.; Torgoev, I.; Ischuk, A. Integrated Geophysical-Geological 3D Model of the Right-Bank Slope Downstream from the Rogun Dam Construction Site, Tajikistan. *Int. J. Geophys.* **2018**, *2018*, 1641789. [[CrossRef](#)]
26. Mreyen, A.S.; Donati, D.; Elmo, D.; Donze, F.V.; Havenith, H.-B. Dynamic numerical modelling of co-seismic landslides using the 3D distinct element method: Insights from the Balta rockslide (Romania). *Eng. Geol.* **2022**, *307*, 106774. [[CrossRef](#)]
27. Lipman, P.W.; Lockwood, J.P.; Okamura, R.T.; Swanson, D.A.; Yamashita, K.M. Ground deformation associated with the 1975 Magnitude-7.2 earthquake and resulting changes in activity of Kilauea volcano, Hawaii. In *The USGS Professional Paper 1276*; Gyan Books Pvt. Ltd.: Delhi, India, 1985; p. 45. [[CrossRef](#)]
28. Hildenbrand, A.; Marques, F.; Catalao, J.; Catita, C.; Costa, A. Large scale active slump of the southeastern flank of Pico Island, Azores. *Geology* **2012**, *40*, 939–942. [[CrossRef](#)]
29. Blahút, J.; Baroň, I.; Sokol, L.; Meletlidis, S.; Klimeš, J.; Rowberry, M.; Melichar, R.; García-Cañada, L.; Martí, X. Large landslide stress states calculated during extreme climatic and tectonic events on El Hierro, Canary Islands. *Landslides* **2018**, *15*, 1801–1814. [[CrossRef](#)]
30. Blahút, J.; Olejár, F.; Rott, J.; Petružálek, M. Current stability modelling of an incipient San Andrés giant landslide on El Hierro, Canaries, Spain—First attempt using limited input data. *Acta Geodyn. Geomat.* **2020**, *17*, 89–99. [[CrossRef](#)]
31. Blahút, J.; Balek, J.; Eliaš, M.; Meletlidis, S. 3D Dilatometer time-series analysis for a better understanding of the dynamics of a giant slow-moving landslide. *App. Sci.* **2020**, *10*, 5469. [[CrossRef](#)]
32. Schmincke, H.-U.; Sumita, M. *Geological Evolution of the Canary Islands*; Görres Druckerei und Verlag: Koblenz, Germany, 2010.
33. Becerril, L.; Galindo, I.; Martí, J.; Gudmundsson, A. Three-armed rifts or masked radial pattern of eruptive fissures? The intriguing case of El Hierro volcano (Canary Islands). *Tectonophysics* **2015**, *647*, 33–47. [[CrossRef](#)]
34. Guillou, H.; Carracedo, J.C.; Pérez Torrado, F.; Rodríguez Badiola, E. K-Ar ages and magnetic stratigraphy of a hotspot-induced, fast grown oceanic island: El Hierro, Canary Islands. *J. Volc. Geotherm. Res.* **1996**, *73*, 141–155. [[CrossRef](#)]
35. Becerril, L.; Ubide, T.; Sudo, M.; Martí, J.; Galindo, I.; Galé, C.; Morales, J.; Yepes, J.; Lago, M. Geochronological constraints on the evolution of El Hierro (Canary Islands). *J. Afr. Earth Sci.* **2016**, *113*, 88–94. [[CrossRef](#)]
36. Risica, G.; Di Roberto, A.; Speranza, F.; Del Carlo, P.; Pompilio, M.; Meletlidis, S.; Todrani, A. Reconstruction of the subaerial Holocene volcanic activity through paleomagnetic and <sup>14</sup>C dating methods: El Hierro (Canary Islands). *J. Volcan. Geotherm. Res.* **2022**, *425*, 107526. [[CrossRef](#)]
37. Stroncik, N.; Klügel, A.; Hansteen, T. The magmatic plumbing system beneath El Hierro (Canary Islands): Constraints from phenocrysts and naturally quenched basaltic glasses in submarine rocks. *Contrib. Miner. Petrol.* **2009**, *157*, 593. [[CrossRef](#)]
38. López, C.; Blanco, M.J.; Abella, R.; Brenes, B.; Cabrera Rodríguez, V.; Casas, B.; Domínguez Cerdeña, I.; Felpeto, A.; Fernández De Villalta, M.; Del Fresno, C.; et al. Monitoring the volcanic unrest of El Hierro (Canary Islands) before the onset of the 2011–2012 submarine eruption. *Geophys. Res. Lett.* **2012**, *39*, L13303. [[CrossRef](#)]
39. Benito-Saz, M.; Parks, M.; Sigmundsson, F.; Hooper, A.; García-Cañada, L. Repeated magmatic intrusions at El Hierro Island following the 2011–2012 submarine eruption. *J. Volcanol. Geotherm. Res.* **2017**, *344*, 79–91. [[CrossRef](#)]
40. Meletlidis, S.; Di Roberto, A.; Domínguez Cerdeña, I.; Pompilio, M.; García-Cañada, L.; Bertagnini, A.; Benito-Saz, M.; Del Carlo, P.; Sainz-Maza Aparicio, S. New insight into the 2011–2012 unrest and eruption of El Hierro Island (Canary Islands) based on integrated geophysical, geodetical, and petrological data. *Ann. Geophys.* **2015**, *58*, S0546. [[CrossRef](#)]
41. Masson, D. Catastrophic collapse of the volcanic island of Hierro 15 ka ago and the history of landslides in the Canary Islands. *Geology* **1996**, *24*, 231–234. [[CrossRef](#)]
42. Urgeles, R.; Canals, M.; Baraza, J.; Alonso, B. The submarine El Golfo debris avalanche and the Canary debris flow, west Hierro Island: The last major slides in the Canary Archipelago. *Geogaceta* **1996**, *20*, 390–393.
43. Urgeles, R.; Canals, M.; Baraza, J.; Alonso, B.; Masson, D. The most recent megalandslides on the Canary Islands: The El Golfo debris avalanche and the Canary debris flow, west El Hierro Island. *J. Geophys. Res. Solid Earth* **1997**, *102*, 20305–20323. [[CrossRef](#)]
44. Carracedo, J.-C.; Day, S.; Guillou, H.; Pérez Torrado, F. Giant quaternary landslides in the evolution of La Palma and El Hierro, Canary Islands. *J. Volcanol. Geotherm. Res.* **1999**, *94*, 169–190. [[CrossRef](#)]

45. Masson, D.; Watts, A.; Gee, M.; Urgeles, R.; Mitchell, N.; Le Bas, T.; Canals, M. Slope failures on the flanks of the western Canary Islands. *Earth Sci. Rev.* **2002**, *57*, 1–35. [[CrossRef](#)]
46. Longpré, M.; Chadwick, J.; Wijbrans, J.; Iping, R. Age of the El Golfo debris avalanche, El Hierro (Canary Islands): New constraints from laser and furnace  $^{40}\text{Ar}/^{39}\text{Ar}$  dating. *J. Volcanol. Geotherm. Res.* **2011**, *203*, 76–80. [[CrossRef](#)]
47. Becerril, L.; Galve, J.; Morales, J.; Romero, C.; Sánchez, N.; Martí, J.; Galindo, I. Volcanostructure of El Hierro (Canary Islands). *J. Maps* **2016**, *12* (Suppl. 1), 43–52. [[CrossRef](#)]
48. Carracedo, J.-C.; Troll, V. *The Geology of Canary Islands*; Elsevier: Amsterdam, The Netherlands, 2016.
49. Blahút, J.; Klimeš, J.; Rowberry, M.; Kusák, M. Database of giant landslides on volcanic islands—First results from the Atlantic Ocean. *Landslides* **2018**, *15*, 823–827. [[CrossRef](#)]
50. Moscardelli, L.; Wood, L. New classification system for mass transport complexes in offshore Trinidad. *Basin Res.* **2008**, *20*, 73–98. [[CrossRef](#)]
51. Klimeš, J.; Yepes, J.; Becerril, L.; Kusák, M.; Galindo, I.; Blahút, J. Development and recent activity of the San Andrés landslide on El Hierro, Canary Islands, Spain. *Geomorphology* **2016**, *261*, 119–131. [[CrossRef](#)]
52. Duffield, W. *Structure and Origin of the Koaie Fault System, Kilauea Volcano, Hawaii*; Professional Paper 856; U.S. Government Publishing Office: Washington, DC, USA, 1975; p. 12.
53. Krastel, S.; Schmincke, H.-U.; Jacobs, C.L.; Rihm, R.; Le Bas, T.P.; Alibés, B. Submarine landslides around the Canary Islands. *J. Geophys. Res. Solid Earth* **2001**, *106*, 3977–3997. [[CrossRef](#)]
54. Gómez Sainz de Aja, J.; Klein, E.; Ruiz García, M.; Balcells Herrera, R.; Del Pozo, M.; Galindo, E.; La Moneda, E. *Mapa Geológico de España, Escala 1:25 000, Valverde (Isla de El Hierro), Hoja N° 1105-II, Memoria*; Instituto Geológico y Minero de España: Madrid, Spain, 2010; p. 96.
55. Troll, V.; Carracedo, J.C. (Eds.) The Geology of El Hierro. In *The Geology of Canary Islands*; Elsevier: Amsterdam, The Netherlands, 2016; pp. 43–99.
56. Blahút, J.; Klimeš, J.; Meletlidis, S.; Balek, J.; Rowberry, M.; Baroň, I. A decade of monitoring and research on the San Andrés megalandslide on El Hierro, Canary Islands, Spain. In *Advances in Natural Hazards and Volcanic Risks: Shaping a Sustainable Future—Proceedings of the 3rd International Workshop on Natural Hazards (NATHAZ22), Terceira Island—Azores 2022*; Springer ASTI Series; Springer: Berlin/Heidelberg, Germany, 2022.
57. MDT05 Modelo Digital del Terreno de España. Sheet PNOA-MDT05-REGCAN95-HU28-1105-1108-LID.ASC. 2015. Available online: <https://centrodedescargas.cnig.es/CentroDescargas> (accessed on 13 March 2018).
58. Instituto Hidrográfico de la Marina, Cuartel General de la Armada, Spain. IHM Bathymetric Data of the Canary Islands. 2016. Available online: <http://portal.emodnet-bathymetry.eu> (accessed on 1 January 2018).
59. Nakamura, Y. A method for dynamic characteristics estimation of subsurface using microtremor on the ground surface. *Railw. Tech. Res. Inst. Quart. Rep.* **1989**, *30*, 25–33.
60. Ibs-von Seht, M.; Wohlenberg, J. Microtremor measurements used to map thickness of soft sediments. *Bull. Seism. Soc. Am.* **1999**, *89*, 250–259. [[CrossRef](#)]
61. Capon, J. High-resolution frequency-wavenumber spectrum analysis. *Proc. IEEE* **1969**, *57*, 1408–1418. [[CrossRef](#)]
62. Rost, S.; Thomas, C. Array seismology: Methods and applications. *Rev. Geophys.* **2002**, *40*, 1–2. [[CrossRef](#)]
63. Wathelet, M.; Chatelain, J.L.; Cornou, C.; Giulio, G.D.; Guillier, B.; Ohrnberger, M.; Savvaidis, A. Geopsy: A user-friendly open-source tool set for ambient vibration processing. *Seismol. Res. Lett.* **2020**, *91*, 1878–1889. [[CrossRef](#)]
64. Shen, C.; Xu, Y.; Pan, Y.; Wang, A.; Gao, L. Sensitivities of phase-velocity dispersion curves of surface waves due to high-velocity-layer and low-velocity-layer models. *J. Appl. Geophys.* **2016**, *135*, 367–374. [[CrossRef](#)]
65. Guedes, V.J.C.B.; Borges, W.R.; Da Cunha, L.S.; Maciel, S.T.R. Characterization of an earth dam in Brazil from seismic refraction tomography and multichannel analysis of surface waves. *J. Appl. Geophys.* **2023**, *208*, 104893. [[CrossRef](#)]
66. Hayashi, K. Data Acquisition and Analysis of Active and Passive Surface Waves. In *Symposium on the Application of Geophysics to Environmental and Engineering Problems Short Course Notes*; Environmental and Engineering Geophysical Society: Denver, CO, USA, 2003; p. 106.
67. Marinos, P.; Hoek, E. GSI: A geologically friendly tool for rock mass strength estimation. In *Proceedings of the GeoEng2000 at the International Conference on Geotechnical and Geological Engineering, Lancaster, PA, USA, 19–24 November 2000*; Technomic Publishers: Lancaster, PA, USA, 2000.
68. Becerril, L. Volcano-Structural Study and Long-Term Volcanic Hazard Assessment on El Hierro Island (Canary Islands). Ph.D. Thesis, University of Zaragoza, Zaragoza, Spain, 2014; ISBN 978-84-617-3444-3.
69. ISRM. *The Complete ISRM Suggested Methods for Rock Characterization, Testing and Monitoring: 1974–2006*; Ulusay, R., Hudson, J.A., Eds.; ISRM: Ankara, Turkey, 2007.
70. Cai, M.; Kaiser, P.K.; Tasaka, Y.; Minami, M. Determination of residual strength parameters of jointed rock masses using the GSI system. *Int. J. Rock Mech. Min. Sci.* **2007**, *44*, 247–265. [[CrossRef](#)]
71. Hoek, E.; Carranza-Torres, C.; Corkum, B. Hoek-Brown Failure Criterion—2002 Edition. In *Proceedings of the NARMS-Tac, Toronto, ON, Canada, 4–6 November 2002*; Volume 1, pp. 267–273.
72. Sapia, V.; Oldenborger, G.A.; Jørgensen, F.; Pugin, A.J.-M.; Marchetti, M.; Viezzoli, A. 3D modeling of buried valley geology using airborne electromagnetic data. *Interpretation* **2015**, *3*, SAC9–SAC22. [[CrossRef](#)]

73. Davarpanah, S.M.; Ván, P.; Vásárhelyi, B. Investigation of the relationship between dynamic and static deformation moduli of rocks. *Geomech. Geophys. Geo-Energy Geo-Resour.* **2020**, *6*, 29. [[CrossRef](#)]
74. Al-Harhi, A.A.; Al-Amri, R.M.; Shehata, W.M. The porosity and engineering properties of vesicular basalt in Saudi Arabia. *Eng. Geol.* **1999**, *54*, 313–320. [[CrossRef](#)]
75. Read, S.A.L.; Richards, L.R. Guidelines for use of tensile data in the calculation of the Hoek-Brown constant  $m_i$ . In Proceedings of the ISRM Congress, Montreal, QC, Canada, 10–14 May 2015; pp. 10–13.
76. Hoek, E. *Practical Rock Engineering*; Rocscience: Toronto, ON, Canada, 2007; p. 342.
77. Marions, P.G.; Marinos, V.; Hoek, E. The Geological Strength Index (GSI): A characterization tool for assessing engineering properties of rock masses. In Proceedings of the International Workshop on Rock Mass Classification in Underground Mining, Vancouver, BC, Canada, 13–18 July 2007. [[CrossRef](#)]
78. Chalupa, V.; Pánek, T.; Tábořík, P.; Klimeš, J.; Hartvich, F.; Grygar, R. Deep-seated gravitational slope deformations controlled by the structure of flysch nappe outlier: Insights from large scale electrical resistivity tomography survey and LiDAR mapping. *Geomorphology* **2018**, *321*, 174–187. [[CrossRef](#)]
79. Tang, C.L.; Hu, J.C.; Lin, M.L.; Angelier, J.; Lu, C.Y.; Chan, Y.C.; Chu, H.T. The Tsaoiling landslide triggered by the Chi-Chi earthquake, Taiwan: Insights from a discrete element simulation. *Eng. Geol.* **2009**, *106*, 1–19. [[CrossRef](#)]
80. Lemaire, E.; Mreyen, A.-S.; Dufresne, A.; Havenith, H.-B. Analysis of the influence of structural geology on the massive seismic slope failure potential supported by numerical modelling. *Geosciences* **2020**, *10*, 323. [[CrossRef](#)]

**Disclaimer/Publisher’s Note:** The statements, opinions and data contained in all publications are solely those of the individual author(s) and contributor(s) and not of MDPI and/or the editor(s). MDPI and/or the editor(s) disclaim responsibility for any injury to people or property resulting from any ideas, methods, instructions or products referred to in the content.